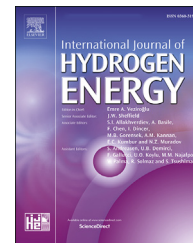




ELSEVIER

Available online at www.sciencedirect.com

ScienceDirect

journal homepage: www.elsevier.com/locate/he

Substitutional effect of Ti-based AB₂ hydrogen storage alloys: A density functional theory study

Siow Mean Loh^{*}, David M. Grant, Gavin S. Walker, Sanliang Ling^{**}

Advanced Materials Research Group, Faculty of Engineering, University of Nottingham, Nottingham, NG7 2RD, UK

HIGHLIGHTS

- Formation energies of substituted AB₂ alloys generally increase with the unit cell volumes of alloys.
- Hydrogenation enthalpies of AB₂ alloys can be tuned to a wide range by substitution.
- Enthalpies of AB₂ hydrides increase with increasing average electronegativity and volume change upon hydrogenation.
- Enthalpies of AB₂ hydrides decrease with increasing average atomic and covalent radii.

ARTICLE INFO

Article history:

Received 26 August 2022

Received in revised form

21 November 2022

Accepted 7 December 2022

Available online xxx

Keywords:

Hydrogen storage

AB₂ alloy

Substitution

Formation energy

Hydrogenation enthalpy

ABSTRACT

Stability of AB₂ alloy in Laves phases C14 and C15 were studied by first-principle density functional theory simulations. A range of different combinations of B and C elements in the Ti_{1-x}C_xB₂ alloys were considered. The formation energies of these alloys generally increase with the unit cell volumes of alloys. The volume also affects the stability of the corresponding metal hydride. We find that the formation energies and the hydrogenation enthalpies of AB₂ alloys are likely to be determined by at least three factors: electronegativity, atomic radius and covalent radius. The enthalpies of AB₂ hydrides increase with increasing compositionally-averaged electronegativity and volume change upon hydrogenation. However, the enthalpies of AB₂ hydrides decrease with increasing compositionally-averaged atomic and covalent radii. This study provides useful insights for future exploration of AB₂-type alloys for hydrogen storage applications.

© 2022 The Author(s). Published by Elsevier Ltd on behalf of Hydrogen Energy Publications LLC. This is an open access article under the CC BY-NC-ND license (<http://creativecommons.org/licenses/by-nc-nd/4.0/>).

Introduction

Searching for clean fuels is an important topic to alleviate the adverse impact of climate change due to greenhouse effect associated with human activity. Hydrogen, with high chemical energy of 142 MJ kg⁻¹ [1], was proposed as a clean, continuous and renewable energy carrier in many applications [2]. Although green hydrogen production has been

realized commercially by electrocatalysis using renewable energy [2,3], economical and easily accessible hydrogen storage is still an important issue which needs to be addressed.

Alloying has the same effect of catalysts to boost the kinetics of hydrogenation and dehydrogenation, as well as the decrease of activation energy [4,5]. For example, the reactions are different due to the appearance of new phases when Mg is alloyed with other metals [4,6–8]. One of the most studied solid-state hydrogen storage methods is the hydrogenation of

^{*} Corresponding author.

^{**} Corresponding author.

E-mail addresses: Siow.Loh@nottingham.ac.uk (S.M. Loh), Sanliang.Ling@nottingham.ac.uk (S. Ling).

<https://doi.org/10.1016/j.ijhydene.2022.12.083>

0360-3199/© 2022 The Author(s). Published by Elsevier Ltd on behalf of Hydrogen Energy Publications LLC. This is an open access article under the CC BY-NC-ND license (<http://creativecommons.org/licenses/by-nc-nd/4.0/>).

Please cite this article as: Loh SM et al., Substitutional effect of Ti-based AB₂ hydrogen storage alloys: A density functional theory study, International Journal of Hydrogen Energy, <https://doi.org/10.1016/j.ijhydene.2022.12.083>

intermetallic alloys. Intermetallic alloys can reversibly store hydrogen with high volumetric capacities but suffer from relatively low gravimetric capacities [2,9]. Intermetallic compound (formula: AB_n) is a family of materials with two or more metal elements, of which A-metal and B-metal tend to form stable and unstable hydrides, respectively [10,11]. Many of them are capable of operating at near ambient temperature conditions, e.g. TiFe (a prototypical AB alloy) [12–15] and LaNi_5 (a prototypical AB_5 alloy) [16–20].

Laves phase AB_2 alloys have been shown to have good performance in properties such as hydrogen storage capacity (e.g. up to 2.2 wt% in $(\text{Ti}_{0.65}\text{Zr}_{0.35})_{1.1}\text{MnCr}_{0.8}\text{Fe}_{0.2}$ [21]), kinetics (e.g. fast kinetics in $\text{Ti}_{0.98}\text{Zr}_{0.02}\text{Cr}_{0.05}\text{V}_{0.43}\text{Fe}_{0.09}\text{Mn}_{1.5}$ [22]) and cycling life (e.g. AB_2 alloys with $A = \text{Ti} + \text{Zr}$ and $B = \text{Mn} + \text{V} + \text{Fe} + \text{Ni}$ have high cyclic stability after 500 cycles [23]). However, the hydrogen capacities of many Laves phase AB_2 alloys are limited to less than 2 wt% for room temperature hydrides. Alloys in the C14 Laves phase (hexagonal structure) possess better performance in storage capacity, charge retention, and cycle stability [24,25]. However, their performance on activation and high-rate dischargeability, is worse than C15 Laves phase (face-centred cubic structure) [24,25]. In addition, hydrogenation enthalpy can be tuned by metal substitution. For example, the A-site substitution of Zr and B-site substitution of V in TiCr_2 lead to the decrease of hydrogenation enthalpies, whereas B-site substitution of Fe shows opposite trend [26]. This is due to different charge transfer between hydrogen and metal atoms. Zr and V behave like electron donors, whereas Fe behaves like electron acceptors [26]. It was found in previous experiment that, the hydrogen capacity increases, hydrogen sorption plateau pressure decreases, absorption kinetics is accelerated, and desorption kinetics is decelerated due to the Zr substitution [27].

The optimal combination of elements in AB_2 alloys for a chosen hydrogen storage application (under certain experimental conditions) can not be easily identified. Although machine learning techniques [28,29] have been used to correlate the materials properties with weighted averages of elemental properties, it will be beneficial to first correlate these properties with atomic parameters without running expensive first-principles reference calculations, formulating the dataset and doing the time-consuming training in machine learning. In this work, we have studied the likelihood of forming Ti-based AB_2 alloys with different metal elements via density functional theory (DFT) calculations. Alloys containing titanium were shown to provide good properties in hydrogen storage, such as high hydrogen absorption capacity (about 3.76 wt%) at 300 K for Ti–6Al–4V alloy [30]. We studied the formation energies of AB_2 alloys in both C14 and C15 phases (see Fig. 1) with a combination of titanium (as A atom) and different B elements, as well as substituted C and D elements in $\text{Ti}_{1-x}\text{C}_x\text{B}_2$ and $\text{TiB}_{2(1-y)}\text{D}_{2y}$ alloys (x and y refer to the substitution concentrations). Next, the substitute distributions in the alloys and its effect on the stability of metal hydrides is considered. Finally, the stabilities of the metal hydrides are discussed. This DFT study thus provides useful guidelines for choosing a metal alloy composition with the right thermodynamic properties in hydrogen storage applications with specified experimental and operating conditions (e.g. temperature and pressure).

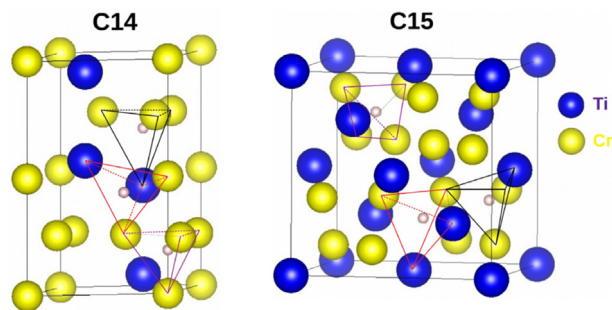


Fig. 1 – Atomic structures of TiCr_2 hydrides in the C14 and C15 phases. Ti, Cr and H are shown in blue, yellow and white colours, respectively. Three compositionally different tetrahedrons (with hydrogen atoms in the centre) are indicated in red (A_2B_2), black (AB_3) and purple (B_4) colours, respectively. (For interpretation of the references to color/colour in this figure legend, the reader is referred to the Web version of this article.)

Computational details

The Vienna Ab initio Simulation Package (VASP) [31–34] was used to calculate the formation energies of AB_2 alloys and the enthalpies of metal hydrides. Perdew-Burke-Ernzerhof (PBE) functional [35] with the projector augmented wave (PAW) [36,37] method was adopted. Due to the large number of compositions which need to be probed, relatively moderate computational settings were used. We anticipate these settings will provide a reasonably accurate qualitative description on our target properties, e.g. alloy formation energies and hydrogenation enthalpies. A plane-wave energy cutoff of 400 eV with a k-point spacing of $\sim 0.2 \text{ \AA}^{-1}$ in the Brillouin zone were chosen. The partial occupancy around each orbital was determined by the first-order Methfessel-Paxton [38] method with a smearing width of 0.2 eV. Structural optimisations were performed with a force tolerance of 0.05 eV/Å and an energy tolerance of 1×10^{-4} eV in the electronic minimisation steps. The C14 Laves phase in a $2 \times 2 \times 1$ supercell (48 atoms) and the C15 Laves phase in a unit cell (24 atoms) were considered in the alloy calculations. For substituted metal alloy compositions, random metal distributions were assumed. Several substitution concentrations x and y from 0.10 to 0.38 were considered for $\text{Ti}_{1-x}\text{C}_x\text{B}_2$ and $\text{TiB}_{2(1-y)}\text{D}_{2y}$ in the calculations. Elements Cr and V were considered as the base atom at the B-site, while Mn and Fe were also considered as B atoms combined with a smaller number of C elements in the $\text{Ti}_{1-x}\text{C}_x\text{B}_2$ alloys. For substitution at the A-site, a range of elements were considered, including [Li, Be, B, Na, Mg, Al, Si, K, Ca, Sc, V, Rb, Sr, Y, Zr, Nb, Tc, Ru, Rh, Ba, Hf, W, Ir, Ce, Pr, U]. For substitution at the B-site, a range of elements were considered, including [Be, B, Mg, Al, Si, V, Mn, Fe, Co, Ni, Cu, Zn, Ga, Ge, As, Se, Mo, Ru, Rh, Pd, Cd, In, Sn, Sb, Hg, Tl, Pb]. The Pauling electronegativity, atomic radius and covalent radius used in this work were based on three references [39–41]. The order of inserting a hydrogen atom into the tetrahedral hole is based on to the magnitude of average electronegativity of the atoms in each tetrahedron. The hydrogen atoms are inserted from the

lowest average electronegativity in A_2B_2 tetrahedral holes to the highest average electronegativity in B_4 tetrahedral holes (see Fig. 1) [28] and the distance of two hydrogen atoms is restricted to be larger than 1.4 Å in the optimised alloy structure (smaller than the distances of 1.8 Å in Ref. [28] and 1.6 Å in Ref. [42]).

The atomic structures of AB_2 alloys in C14 and C15 phases are shown through Visualization for Electronic and STructural analysis (VESTA) software [43] as in Fig. 1.

Results and discussions

Formation energies of $Ti_{1-x}C_xB_2$ and $TiB_{2(1-y)}D_{2y}$ alloys

Factors influencing the formation energies of metal alloys

Formation energy is an important parameter to indicate the stability of a compound. The formation energies E_F of the $Ti_{1-x}C_xB_2$ and $TiB_{2(1-y)}D_{2y}$ alloys with respect to the non-substituted TiB_2 alloy are defined as [44,45].

$$E_F = E_T^{AB_2'} - E_T^{AB_2} - n\mu_{Ti} + n\mu_C \quad (1)$$

$$E_F = E_T^{AB_2'} - E_T^{AB_2} - n\mu_B + n\mu_D \quad (2)$$

where $E_T^{AB_2'}$ and $E_T^{AB_2}$ refer to the total energies of $Ti_{1-x}C_xB_2$ (or $TiB_{2(1-y)}D_{2y}$) and TiB_2 alloys, respectively, n and μ_i refer to the number of substituted atoms and the chemical potential of atom i taken from the elemental crystal.

The formation energies of most of the $Ti_{1-x}C_xCr_2$ alloys in C14 and C15 phases considered in this work are related to the

volume change ($\Delta V = V_{AB_2'} - V_{AB_2}$) of the cells after the substitution for Ti (Fig. 2(a)). The formation energies of most of the alloys shown in empty symbols increase as ΔV increases within each row of the periodic table. Since the volume change is related to the change of atomic radius r_a , the formation energy also increases as the atomic radius of C atom increases (Fig. 2(b)). Because the trend of electronegativity in the same row of the periodic table is opposite to that of the atomic radius (e.g. in the fourth row of the periodic table, the electronegativity increases from K to Kr, however, the atomic radius decreases at the same time), the formation energy also increases as the electronegativity decreases. Similar results can also be seen for V, Mn and Fe as B atom at different substitution concentrations ($x = 0.125-0.375$).

The formation energies of B-atom substituted $TiB_{2(1-y)}D_{2y}$ alloys do not increase as the volume/atomic radii increase (see Figs. 1 and 2 in supplementary material). Other factors, such as the difference in the electron density at the Wigner-Seitz cell boundary and the atomic size in the alloys reported in Ref. [46] which are not considered here, may explain the exceptions (including some $Ti_{1-x}C_xCr_2$ alloys not shown in Fig. 2 and $TiB_{2(1-y)}D_{2y}$ alloys). It is worth noting that the resulting formation energy for the same C atom at $x = 0.125$ is similar for C14 and C15 phases (Fig. 2(b)).

Formation energies of metal alloys vs substitution concentration

Fig. 3 shows that the formation energy increases as the substitution concentration increases if the substitution of the atoms leads to the increase of formation energy, and vice versa. This observation also applies to other $Ti_{1-x}C_xB_2$ and $TiB_{2(1-y)}D_{2y}$ alloys. Therefore, an alloy which can be stably

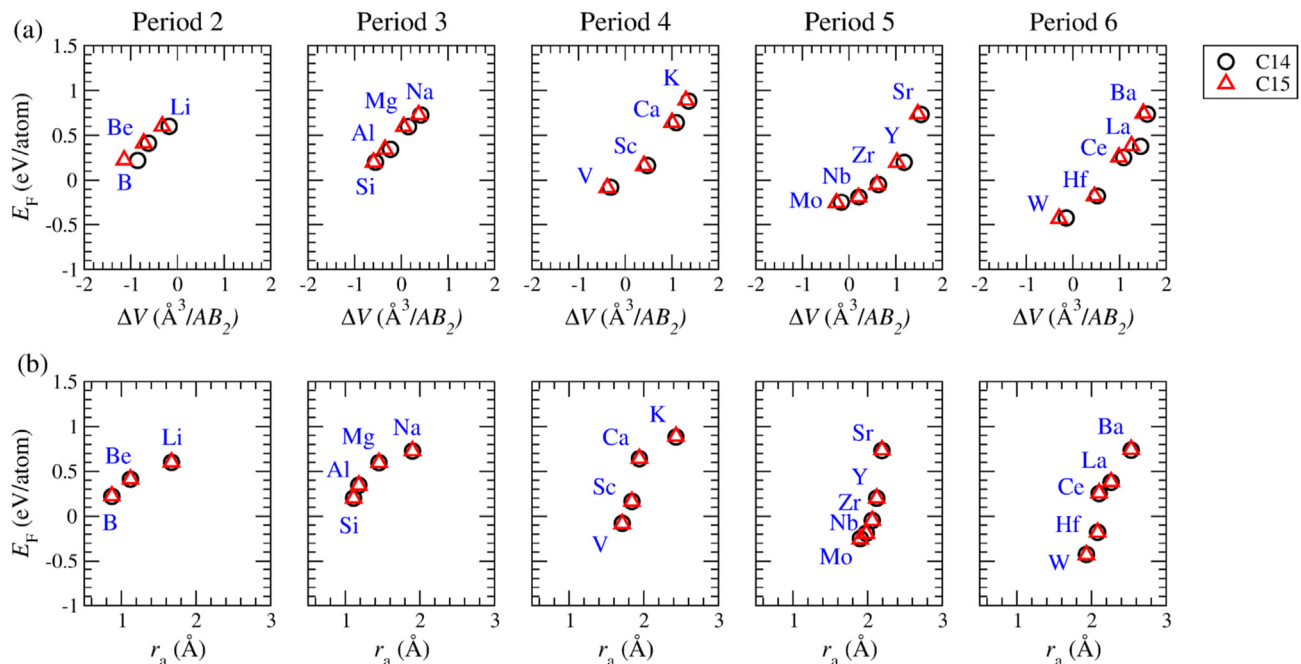


Fig. 2 – Formation energy of $Ti_{1-x}C_xCr_2$ alloy vs volume change due to substitution and atomic radius of C atom. Formation energy (E_F) as a function of (a) volume change per formula unit ($\Delta V = V_{Ti_{0.875}C_{0.125}Cr_2} - V_{TiCr_2}$) (b) atomic radius of C atom for $Ti_{0.875}C_{0.125}Cr_2$ alloys in the C14 and C15 phases. Black circles and red triangles refer to the AB_2 alloys in C14 and C15 phases, respectively. Each C atom belonging to the same row of the periodic table is plotted in the same subfigure. (For interpretation of the references to color/colour in this figure legend, the reader is referred to the Web version of this article.)

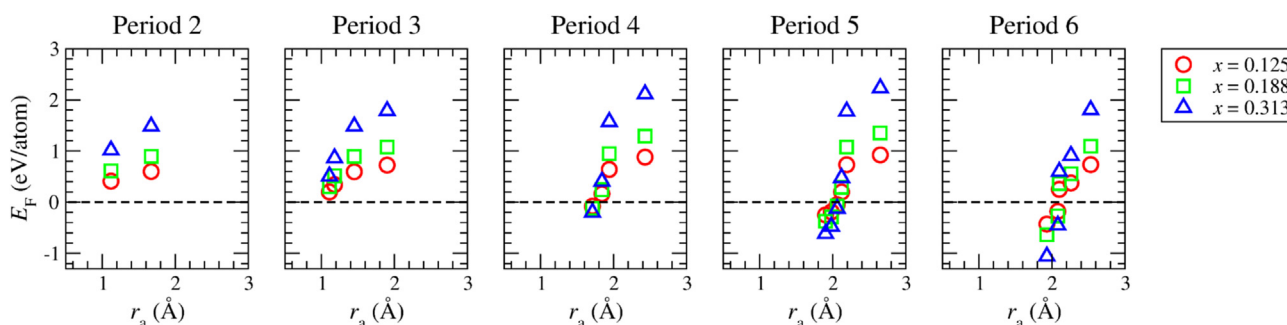


Fig. 3 – Formation energy of $\text{Ti}_{1-x}\text{C}_x\text{Cr}_2$ alloy vs atomic radius of C atom. Formation energy (E_F) as a function of the atomic radius of C atom for $\text{Ti}_{1-x}\text{C}_x\text{Cr}_2$ ($x = 0.125, 0.188$ and 0.313) alloys in the C14 phase. Red circles, green squares and blue triangles refer to the $\text{Ti}_{1-x}\text{C}_x\text{Cr}_2$ alloys at $x = 0.125$, $x = 0.188$ and $x = 0.313$, respectively. Each C atom belonging to the same row of the periodic table is plotted in the same subfigure. (For interpretation of the references to color/colour in this figure legend, the reader is referred to the Web version of this article.)

formed after substitution (represented as negative formation energy) becomes more stable after further substitutions.

Furthermore, whether a substitute atom prefers to substitute for A or B atom depends on the average atomic radius of the resulting alloy based on our limited study. If the compositionally-averaged atomic radius of $\text{Ti}_{1-x}\text{C}_x\text{B}_2$ alloy is smaller than that of $\text{TiB}_{2(1-y)}\text{D}_{2y}$ alloy, the formation of $\text{Ti}_{1-x}\text{C}_x\text{B}_2$ is preferred. The reason may be explained by the same finding in Fig. 2: C atom with smaller atomic radius forms more stable $\text{Ti}_{1-x}\text{C}_x\text{B}_2$ alloy. This observation applies to our calculations including substitute C or D atoms = Be, Si, Mg, V, Mo, Ru, Rh and B atom = Cr, V and Sc. For example, if we take Mg as C atom in the $\text{Ti}_{1-x}\text{C}_x\text{B}_2$ alloy and D atom in the $\text{TiB}_{2(1-y)}\text{D}_{2y}$ alloy in C14 phase with substituted concentration $x \approx 0.2$ and $y \approx 0.1$, we can find [average atomic radius, formation energy] = [1.674 Å, 0.893 eV/atom] for the $\text{Ti}_{0.8}\text{Mg}_{0.2}\text{Cr}_2$ alloy and [average atomic radius, formation energy] = [1.680 Å, 1.136 eV/atom] for the $\text{TiCr}_{1.8}\text{Mg}_{0.2}$ alloy, respectively. This leads to Mg substitute for Ti rather than Cr. If we consider Sc as B atom, we can find [average atomic radius, formation energy] = [1.794 Å, 0.475 eV/atom] for the $\text{Ti}_{0.8}\text{Mg}_{0.2}\text{Sc}_2$ alloy and [average atomic radius, formation energy] = [1.789 Å, 0.376 eV/atom] for the $\text{TiSc}_{1.8}\text{Mg}_{0.2}$ alloy. This leads to Mg substitution for Sc rather than Ti. Note that TiSc_2 may not be a realistic AB_2 alloy, it is chosen only for demonstrating smaller average atomic radius in $\text{TiB}_{2(1-y)}\text{D}_{2y}$.

Substitute distribution of metal alloy

$\text{Ti}_{1-x}\text{C}_x\text{B}_2$ alloys with random distributions of Ti and C metals were used in the calculations based on the assumption that the temperature is high during the synthesis experiment. Thus, it would be interesting to know how likely the clustered substitute distribution can be formed for different alloy compositions and its role on the hydride stability.

The ΔE_F of different alloys as a function of electronegativity of C atom were shown in Fig. 4, where ΔE_F is defined as the difference of formation energy between $\text{Ti}_{1-x}\text{C}_x\text{B}_2$ alloys with clustered substitute distribution and isolated substitute distribution [47]. Note that in the clustered substitute distribution, the substituted C atoms were placed at the nearest distances among all A-site positions. This includes Sr, Ca, Mg

and Zr as C atom and V, Cr, Mn and Fe as B atom. In general, the negative ΔE_F increases as the electronegativity of C atom increases (see the cases for B atom = Cr, Mn and Fe). In contrast, the positive ΔE_F decreases as the electronegativity of C atom increases (see the cases for B atom = V). Of the largest atomic radius among these four B atoms (V, Cr, Mn and Fe), vanadium has a similar atomic radius to A atom, titanium. This may be the reason why we see isolated substitute distribution in this alloy. The substitute atoms are more likely to segregate if C atom has lower electronegativity ($\chi_p \leq 1.00$) when the base atom at B-site is Cr, Mn and Fe. This may be due to the larger difference of electronegativity between these C metals and Ti. The trend of ΔE_F as a function of electronegativity of C atom looks similar in C14 and C15 phases.

Although the difference of formation energies between clustered and isolated substitute distributions is significant, the difference in their hydrogenation enthalpies is small. $\text{Ti}_{1-x}\text{Sr}_x\text{Mn}_2$ has the largest difference of formation energy ΔE_F between clustered and isolated distributions (at $\chi_p = 0.95$) in Fig. 4, however, the differences of hydrogenation enthalpies are only about 0.21% and 0.34% for C14 and C15 phases, respectively. Thus, the substitute distribution may not play a significant role in the stability of $\text{Ti}_{1-x}\text{C}_x\text{B}_2$ hydride.

Hydrogenation enthalpies of $\text{Ti}_{1-x}\text{C}_x\text{B}_2$ and $\text{TiB}_{2(1-y)}\text{D}_{2y}$ alloys

Factors influencing the enthalpies of metal hydrides

For hydrogen storage, the enthalpy which determines the stability of hydrogen stored in an alloy is as important as the stability of the alloy (formation energy discussed in section 3.1). The hydrogenation enthalpy of an AB_2 alloy is defined as [29,48].

$$\Delta H = \frac{1}{n} \left(E_{\text{AB}_2\text{H}_n} - E_{\text{AB}_2} - \frac{n}{2} E_{\text{H}_2} \right) \quad (3)$$

where $E_{\text{AB}_2\text{H}_n}$, E_{AB_2} , E_{H_2} and n are the total energy of an AB_2 hydride with n hydrogen atoms, total energy of an AB_2 alloy, total energy of hydrogen gas and number of hydrogen atoms, respectively. In Fig. 5(a)-(c), the hydrogenation enthalpy mostly depends on the compositionally-averaged atomic

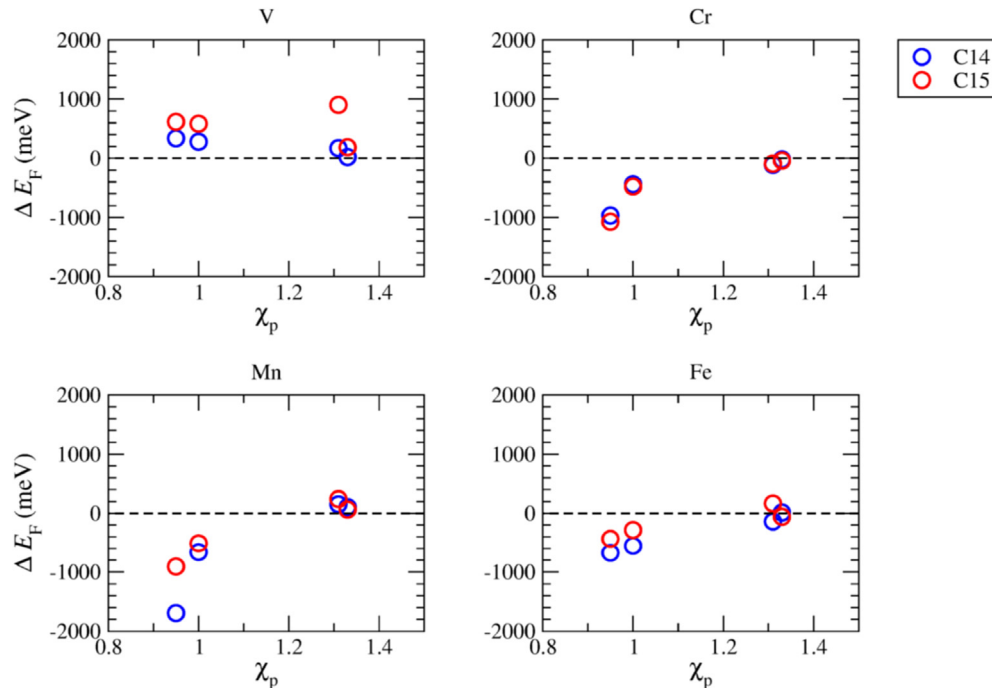


Fig. 4 – Comparison of formation energy between clustered and isolated substitute distributions. ΔE_F (E_F (clustered dopants) - E_F (isolated dopants)) of various $Ti_{1-x}C_xB_2$ alloys in C14 (blue) and C15 (red) phases as a function of the electronegativity of C atom. The titles above each subfigure refer to different B atom in $Ti_{1-x}C_xB_2$ alloy. (For interpretation of the references to color/colour in this figure legend, the reader is referred to the Web version of this article.)

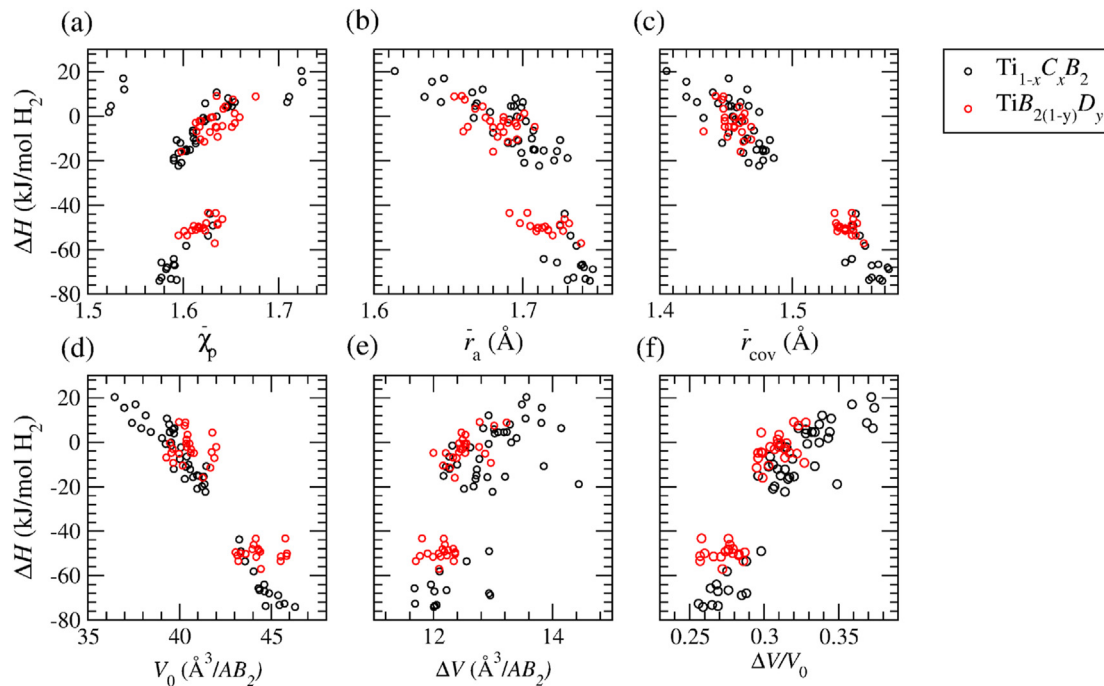


Fig. 5 – Hydrogenation enthalpy vs average electronegativity, atomic radius, covalent radius and cell volume in the AB_2 alloys. Enthalpy of metal hydride with a H/M ratio of 1.79 for $Ti_{0.875}C_{0.125}B_2$ (black) and $TiB_{1.812}D_{0.188}$ (red) alloys in the C14 phase as a function of (a) average electronegativity ($\bar{\chi}_p$) (b) average atomic radius (\bar{r}_a) (c) average covalent radius (\bar{r}_{cov}) (d) volume of alloy (V_0) (e) volume expansion (per formula unit) upon hydrogenation (ΔV) (f) ratio of volume expansion upon hydrogenation to volume of alloy ($\Delta V/V_0$). A high H/M ratio of 1.79 is considered for the hydride, thus significantly reducing the effect of energy difference due to hydrogen absorption in the tetrahedral holes with different combinations of elements on the comparison. (For interpretation of the references to color/colour in this figure legend, the reader is referred to the Web version of this article.)

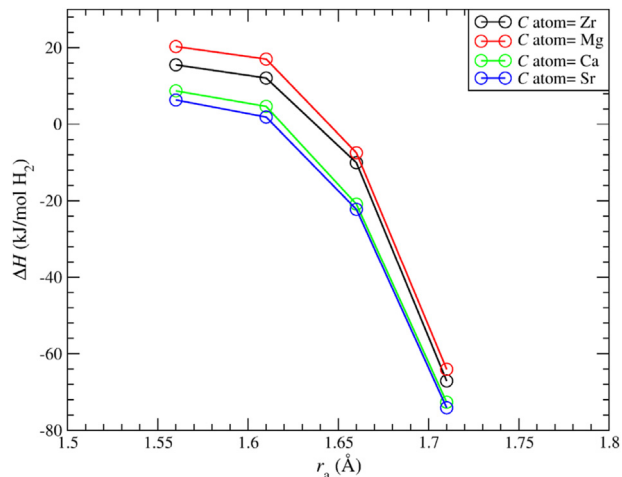


Fig. 6 – Hydrogenation enthalpy vs atomic radius of various B atoms (include Fe, Mn, Cr, V) in $\text{Ti}_{0.875}\text{C}_{0.125}\text{B}_2$ alloys in the C14 phase, where C atoms include Zr, Mg, Ca and Sr.

radius (\bar{r}_a) and covalent radius (\bar{r}_{cov}) of atoms, whereas the direct effect of average electronegativity of atoms in enthalpy is less pronounced. Generally, the enthalpy decreases as the average atomic radius and average covalent radius increase (associated with a smaller volume expansion upon hydrogenation, see Fig. 5(e)–(f)). In Fig. 5(e)–(f), a larger volume expansion upon hydrogenation leads to a larger enthalpy. A similar result were found by Witman et al. [29] and Westlake [49]. In contrast, the hydrogenation enthalpy increases as the average electronegativity increases.

Our result is in good agreement with previous literature in which the hydrogenation enthalpy was related to the chemical and structural contributions (e.g. bonding, volume expansion [50] and elastic modulus [29]). In AB_2 alloys, hydrogen atoms prefer to occupy the tetrahedral holes composed of atoms with lower average electronegativity in the alloy [28]. However, the influence of the electronegativity which related to the attraction for hydrogen atom is less significant than the volume change upon hydrogenation in determining the stability of the hydrides.

In Fig. 6, the hydrogenation enthalpy increases as the atomic radius of B atom decreases ($\text{Fe} < \text{Mn} < \text{Cr} < \text{V}$) for different $\text{Ti}_{0.875}\text{C}_{0.125}\text{B}_2$ alloys. Similarly, the ZrFe_2 hydride becomes more stable by substituting V for Fe as shown in a previous study [51]. This is possibly because the volume expansion upon hydrogenation is mostly determined by the geometric effect (related to the atomic size) than the chemical effect (related to the attraction for hydrogen atoms). This is in good agreement with a previous study on Zr-based AB_2 alloys [52], in which the authors found that a more stable metal hydride is associated with a larger average atomic size. It is worth noting that the trend of the formation energy of an alloy is opposite to the trend of the enthalpy of metal hydride with increasing atomic radius (Fig. 2(b) and Fig. 5(b)), which agrees well with the findings in previous literatures that the stability of alloy and hydride is opposite [28,29,53]. The hydrogenation enthalpies of different A-site and B-site substitutions discussed in this work were shown in the supplementary material.

To understand the correlation between hydrogenation enthalpy, alloy unit cell volume, and covalent radius, we performed linear regressions of hydrogenation enthalpy as a function of unit cell volume of alloy (V_0) and average covalent

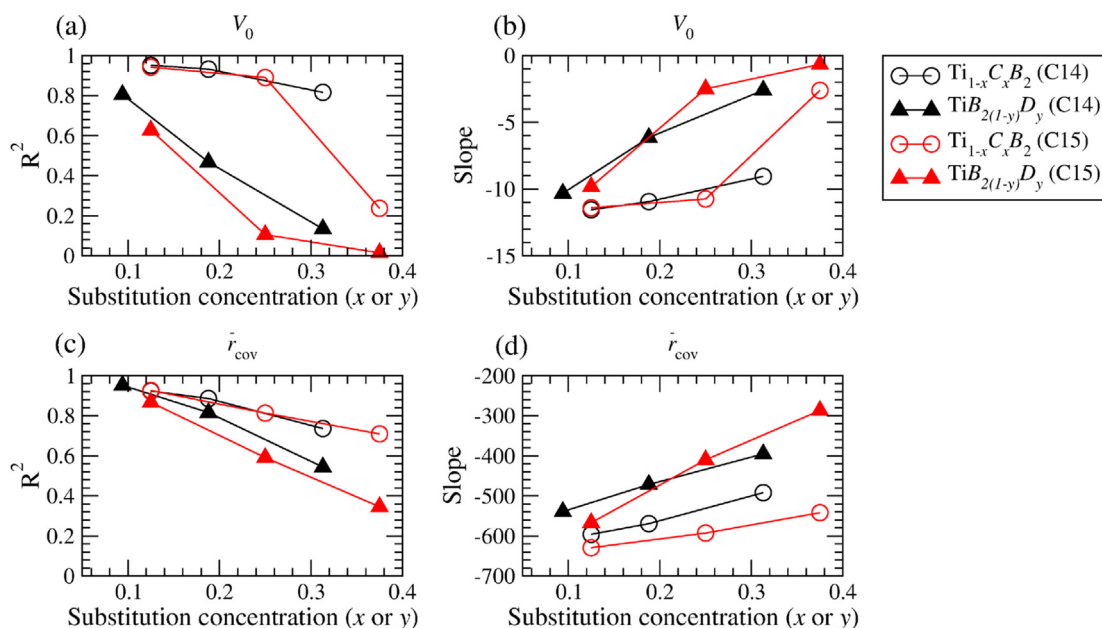


Fig. 7 – Coefficient of determination R^2 and slope of linear regression vs substitution concentration. (a) (c) Coefficient of determination R^2 (b) (d) Slope of linear regression based on hydrogenation enthalpy vs (a) (b) volume of alloy (V_0) and (c) (d) average covalent radius (\bar{r}_{cov}) in Fig. 5. Circle and triangle symbols refer to $\text{Ti}_{1-x}\text{C}_x\text{B}_2$ and $\text{TiB}_{2(1-y)}\text{D}_y$ alloys, respectively. Black and red curves refer to the C14 and C15 phases, respectively. (For interpretation of the references to color/colour in this figure legend, the reader is referred to the Web version of this article.)

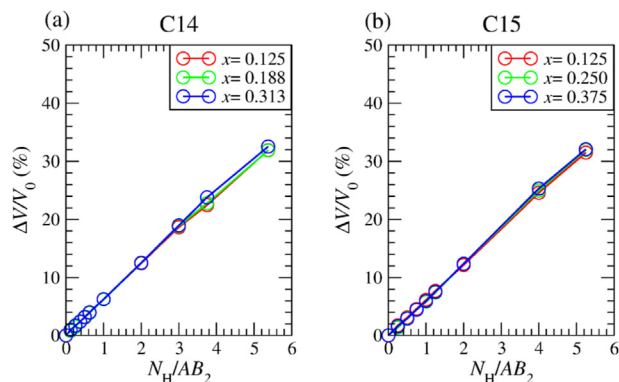


Fig. 8 – Ratio between volume expansion upon hydrogenation and volume of alloy ($\Delta V/V_0$) as a function of number of hydrogen atoms per formula unit (N_H/AB_2) in the (a) C14 phase and (b) C15 phase.

radius (r_{cov}) at different substitution concentrations. The coefficient of determination R^2 of linear regression measures how well a model predicts an outcome. Fig. 7(a) and 7(c) show the coefficient of determination R^2 of linear regression in Fig. 5(c) and (d) as a function of substitution concentration. We can find that the R^2 of linear regression in Fig. 7(a) and 7(c) is high (0.80–0.95) at lower substitution concentration ($x \approx 0.1$ –0.2) for $Ti_{1-x}C_xB_2$ alloy (black and red curves with circle symbol), although the hydrogenation enthalpy was expressed as a polynomial composed of a range of factors including differences of average electronegativity, atomic size, elastic modulus and electron concentration in previous literatures [52,54]. Due to the more dispersed data points, the R^2 of $TiB_{2(1-y)}D_{2y}$ alloy is lower than $Ti_{1-x}C_xB_2$ alloy. Polynomial regression may need to be employed for higher substitution concentrations. The decrease of R^2 with the substitution concentrations x or y may imply that different parameters such as differences of average electronegativity, atomic size, elastic modulus and electron concentration [52,54] originating from the substitute atoms become more important with increasing substitution concentrations.

In Fig. 7(b) and 7(d), the smaller absolute value of slope for $TiB_{2(1-y)}D_{2y}$ alloys compared with $Ti_{1-x}C_xB_2$ alloys in the same phase may imply that $TiB_{2(1-y)}D_{2y}$ alloys are less affected by the average covalent radius and unit cell volume of alloy. The smaller absolute value of slope can also be seen at higher substitution concentrations, implying the lower influence of the average covalent radius and unit cell volume of alloy on hydrogenation enthalpy at higher substitution concentrations.

Magnitude of volume change upon hydrogenation

The magnitude of volume change almost remains at a constant when increasing number of hydrogen atoms in both C14 and C15 phases (Fig. 8). The linear increase in magnitude of $\Delta V/V_0$ with increasing number of hydrogen atoms can also be seen in Ref. [55]. The curve gradually becomes non-linear if we increase the number of hydrogen atoms absorbed because the volume expansion is different when hydrogen atoms are stored in different types of tetrahedral holes. For example, the

$\Delta V/V_0$ is about 0.4% when a hydrogen atom is inserted into a A_2B_2 tetrahedral hole, whereas the $\Delta V/V_0$ is about 0.8% when a hydrogen atom is inserted into a B_4 tetrahedral hole of the $Ti_{0.725}Mg_{0.125}Cr_2$ alloy in C14 phase. This constant magnitude of volume change remains up to $x \approx 0.3$ (the highest substitution concentration considered in this work) for $Ti_{1-x}Mg_xCr_2$, but the magnitude may be different for alloys of different compositions.

Conclusion

The formation energies and the hydrogenation enthalpies of $Ti_{1-x}C_xB_2$ and $TiB_{2(1-y)}D_{2y}$ alloys were discussed in this work. In general, the formation energy of A-site substituted $Ti_{1-x}C_xB_2$ alloy increases with increasing unit cell volume change after substitution and increasing atomic radius of C atom, and decreases with increasing electronegativity of C atom in each row of the periodic table. However, this observation does not apply to the B-site substituted $TiB_{2(1-y)}D_{2y}$ alloys. The stability of the alloy can be further increased by further substitution of Ti by C atoms if the substitution is energetically favourable. The substitute distribution of an alloy has little effect on the hydrogenation enthalpy of metal alloy, although the local substitute segregation may exist in the alloy depending on the electronegativity of the substitute C atom. For example, the enthalpy difference between clustered distribution and isolated distribution of Sr substitute is less than 0.4% for $Ti_{1-x}Sr_xMn_2$ hydrides which has a strong tendency to form clustered distribution.

The hydrogenation enthalpies of $Ti_{1-x}C_xB_2$ and $TiB_{2(1-y)}D_{2y}$ alloys mostly decrease with increasing compositionally-averaged atomic and covalent radii. This is related to the volume expansion upon hydrogenation being inversely proportional to the volume of alloy (see Fig. 5(d) and (e)). The hydrogenation enthalpy is also partly influenced by the average electronegativity (hydrogenation enthalpy increases as the average electronegativity increases).

The linearity of the correlation between hydrogenation enthalpy and covalent radius (or volume of alloy) is obvious at lower substitution concentration ($R^2 > 0.9$ for $Ti_{1-x}C_xB_2$ alloys). The $TiB_{2(1-y)}D_{2y}$ alloys (B-atoms substitution) are less affected by these factors than the $Ti_{1-x}C_xB_2$ alloys (A-atom substitution). In addition, the magnitude of volume change upon hydrogenation almost linearly depends on the number of hydrogen atoms absorbed in the alloy when hydrogen atoms occupy the same type of tetrahedral hole (e.g. A_2B_2). Hydrogen atoms will occupy different types of interstitial holes if the number of hydrogen atoms absorbed increases, leading to the curve in Fig. 8 becoming non-linear at higher hydrogen loading levels. The magnitudes of volume change in the C14 and C15 phases are different, which may be related to the difference in the distribution of different tetrahedral holes in the C14 and C15 phases.

These findings imply that we can choose substituted atoms with smaller atomic size if we want to form a more stable AB_2 alloy, and vice versa. However, we also need to take into consideration that alloys composed of substituted atoms with smaller atomic size will lead to a less stable hydride upon hydrogenation [28,29,53]. Therefore, the optimal alloy

composition for a chosen hydrogen storage application can be more easily predicted based on the relative stability of the alloys and intermetallic hydrides at different experimental conditions, and thus boosting the development of this area.

Supplementary material

DFT predicted formation energies and hydrogenation enthalpies of $Ti_{1-x}C_xB_2$ and $TiB_{2(1-y)}D_y$ ($x = 0.125, 0.188, 0.313, y = 0.094, 0.188, 0.313$ for C14 phase and $x = 0.125, 0.250, 0.375, y = 0.125, 0.250, 0.375$ for C15 phase) alloys were provided.

Declaration of competing interest

The authors declare that they have no known competing financial interests or personal relationships that could have appeared to influence the work reported in this paper.

Acknowledgements

This work is supported by Engineering and Physical Sciences Research Council (EP/V042556/1). The authors acknowledge the use of the Sulis supercomputer through the HPC Midlands Plus Consortium, and the YOUNG and ARCHER2 supercomputers through membership of the U.K.'s HPC Materials Chemistry Consortium, which are funded by EPSRC Grant Nos. EP/T022108/1, EP/T022213/1 and EP/R029431/1, respectively. We thank Samuel Lines for useful comments on the manuscript.

Appendix A. Supplementary data

Supplementary data to this article can be found online at <https://doi.org/10.1016/j.ijhydene.2022.12.083>.

REFERENCES

- [1] Schlapbach L, Züttel A. Hydrogen-storage materials for mobile applications. *Nature* 2001;414:353–8. <https://doi.org/10.1038/35104634>.
- [2] Jain V, Kandasubramanian B. Functionalized graphene materials for hydrogen storage. *J Mater Sci* 2020;55:1865–903. <https://doi.org/10.1007/s10853-019-04150-y>.
- [3] <https://www.energy.gov/eere/fuelcells/hydrogen-production-processes> accessed on 16 November 2022.
- [4] Li Q, Lin X, Luo Q, Chen Y, Wang J, Jiang B, Pan F. Kinetics of the hydrogen absorption and desorption processes of hydrogen storage alloys: a review. *Int. J. Miner. Metall. Mater.* 2022;29:32–48. <https://doi.org/10.1007/s12613-021-2337-8>.
- [5] Zhang J, Yan S, Xia G, Zhou X, Lu X, Yu L, Yu X, Peng P. Stabilization of low-valence transition metal towards advanced catalytic effects on the hydrogen storage performance of magnesium hydride. *J. Magnesium Alloys* 2021;9:647–57. <https://doi.org/10.1016/j.jma.2020.02.029>.
- [6] Xie T, Shi H, Wang H, Luo Q, Li Q, Chou K-C. Thermodynamic prediction of thermal diffusivity and thermal conductivity in Mg–Zn–La/Ce system. *J Mater Sci Technol* 2022;97:147–55. <https://doi.org/10.1016/j.jmst.2021.04.044>.
- [7] Liang G. Synthesis and hydrogen storage properties of Mg-based alloys. *J Alloys Compd* 2004;370:123–8. <https://doi.org/10.1016/j.jallcom.2003.09.031>.
- [8] Yong H, Guo S, Yuan Z, Qi Y, Zhao D, Zhang Y. Improved hydrogen storage kinetics and thermodynamics of RE–Mg-based alloy by co-doping Ce–Y. *Int J Hydrogen Energy* 2019;44:16765–76. <https://doi.org/10.1016/j.ijhydene.2019.04.281>.
- [9] Züttel A. Hydrogen storage methods. *Naturwissenschaften* 2004;91:157–72. <https://doi.org/10.1007/s00114-004-0516-x>.
- [10] Sakintuna B, Lamari-Darkrim F, Hirscher M. Metal hydride materials for solid hydrogen storage: a review. *Int J Hydrogen Energy* 2007;32:1121–40. <https://doi.org/10.1016/j.ijhydene.2006.11.022>.
- [11] Marques F, Balcerzak M, Winkelmann F, Zepon G, Felderhoff M. Review and outlook on high-entropy alloys for hydrogen storage. *Energy Environ Sci* 2021;14:5191–227. <https://doi.org/10.1039/D1EE01543E>.
- [12] Sujan GK, Pan Z, Li H, Liang D, Alam N. An overview on TiFe intermetallic for solid-state hydrogen storage: microstructure, hydrogenation and fabrication processes. *Crit Rev Solid State Mater Sci* 2020;45:410–27. <https://doi.org/10.1080/10408436.2019.1652143>.
- [13] Reilly JJ, Wiswall RH. Formation and properties of iron titanium hydride. *Inorg Chem* 1974;13:218–22. <https://doi.org/10.1021/ic50131a042>.
- [14] Lototskyy MV, Yartys VA, Pollet BG, Bowman Jr RC. Metal hydride hydrogen compressors: a review. *Int J Hydrogen Energy* 2014;39:5818–51. <https://doi.org/10.1016/j.ijhydene.2014.01.158>.
- [15] Tarasov BP, Fursikov PV, Volodin AA, Bocharnikov MS, Shimkus YY, Kashin AM, Yartys VA, Chidziva S, Pasupathi S, Lototskyy MV. Metal hydride hydrogen storage and compression systems for energy storage technologies. *Int J Hydrogen Energy* 2021;46:13647–57. <https://doi.org/10.1016/j.ijhydene.2020.07.085>.
- [16] Joubert J-M, Paul-Boncour V, Cuevas F, Zhang J, Latroche M. LaNi₅ related AB₅ compounds: structure, properties and applications. *J Alloys Compd* 2021;862:158163. <https://doi.org/10.1016/j.jallcom.2020.158163>.
- [17] Liu W, Aguey-Zinsou K-F. Low temperature synthesis of LaNi₅ nanoparticles for hydrogen storage. *Int J Hydrogen Energy* 2016;41:1679–87. <https://doi.org/10.1016/j.ijhydene.2015.10.128>.
- [18] Dhaou H, Askri F, Salah MB, Jemni A, Ben Nasrallah S, Lamloumi J. Measurement and modelling of kinetics of hydrogen sorption by LaNi₅ and two related pseudobinary compounds. *Int J Hydrogen Energy* 2007;32:576–87. <https://doi.org/10.1016/j.ijhydene.2006.07.001>.
- [19] Ngameni R, Mbemba N, Grigoriev SA, Millet P. Comparative analysis of the hydriding kinetics of LaNi₅, La_{0.8}Nd_{0.2}Ni₅ and La_{0.7}Ce_{0.3}Ni₅ compounds. *Int J Hydrogen Energy* 2011;36:4178–84. <https://doi.org/10.1016/j.ijhydene.2010.06.107>.
- [20] Luo S, Clewley JD, Flanagan TB, Bowman Jr RC, Wade LA. Further studies of the isotherms of LaNi_{5-x}Sn_x-H for $x=0-0.5$. *J Alloys Compd* 1998;267:171–81. [https://doi.org/10.1016/S0925-8388\(97\)00536-7](https://doi.org/10.1016/S0925-8388(97)00536-7).
- [21] Manickam K, Grant DM, Walker GS. Optimization of AB₂ type alloy composition with superior hydrogen storage properties for stationary applications. *Int J Hydrogen Energy* 2015;40:16288–96. <https://doi.org/10.1016/j.ijhydene.2015.09.157>.

- [22] Bowman Jr RC, Fultz B. Metallic hydrides I: hydrogen storage and other gas- phase applications. *MRS Bull* 2002;27:688–93. <https://doi.org/10.1557/mrs2002.223>.
- [23] Wijayanti ID, Denys R, Suwarno, Volodin AA, Lototsky MV, Guzik MN, Nei J, Young K, Roven HJ, Yartys V. Hydrides of Laves type Ti–Zr alloys with enhanced H storage capacity as advanced metal hydride battery anodes. *J Alloys Compd* 2020;828:154354. <https://doi.org/10.1016/j.jallcom.2020.154354>.
- [24] Young K-H, Koch JM, Wan C, Denys RV, Yartys VA. Cell performance comparison between C14- and C15- predominated AB₂ metal hydride alloys. *Batteries* 2017;3:29. <https://doi.org/10.3390/batteries3040029>.
- [25] Young K-H, Nei J, Wan C, Denys RV, Yartys VA. Comparison of C14- and C15- predominated AB₂ metal hydride alloys for electrochemical applications. *Batteries* 2017;3:22. <https://doi.org/10.3390/batteries3030022>.
- [26] Li F, Zhao J, Sun L. Substitution effects on the hydrogen storage behavior of AB₂ alloys by first principles. *Front Physiol* 2011;6:214–9. <https://doi.org/10.1007/s11467-011-0172-5>.
- [27] Kandavel M, Bhat VV, Rougier A, Aymard L, Nazri G-A, Tarascon J-M. Improvement of hydrogen storage properties of the AB₂ Laves phase alloys for automotive application. *Int J Hydrogen Energy* 2008;33:3754–61. <https://doi.org/10.1016/j.ijhydene.2008.04.042>.
- [28] Witman M, Ek G, Ling S, Chames J, Agarwal S, Wong J, Allendorf MD, Sahlberg M, Stavila V. Data-driven discovery and synthesis of high entropy alloy hydrides with targeted thermodynamic stability. *Chem Mater* 2021;33:4067–76. <https://doi.org/10.1021/acs.chemmater.1c00647>.
- [29] Witman M, Ling S, Grant DM, Walker GS, Agarwal S, Stavila V, Allendorf MD. Extracting an empirical intermetallic hydride design principle from limited data via interpretable machine learning. *J Phys Chem Lett* 2020;11:40–7. <https://doi.org/10.1021/acs.jpcclett.9b02971>.
- [30] Blackburn JL, Parilla PA, Gennett T, Hurst KE, Dillon AC, Heben MJ. Measurement of the reversible hydrogen storage capacity of milligram Ti–6Al–4V alloy samples with temperature programmed desorption and volumetric techniques. *J Alloys Compd* 2008;454:483–90. <https://doi.org/10.1016/j.jallcom.2007.01.006>.
- [31] Kresse G, Hafner J. Ab initio molecular dynamics for liquid metals. *Phys Rev B* 1993;47:558. <https://doi.org/10.1103/PhysRevB.47.558> (R).
- [32] Kresse G, Hafner J. Ab initio molecular-dynamics simulation of the liquid-metal-amorphous-semiconductor transition in germanium. *Phys Rev B* 1994;49:14251. <https://doi.org/10.1103/PhysRevB.49.14251>.
- [33] Kresse G, Furthmüller J. Efficiency of ab-initio total energy calculations for metals and semiconductors using a plane-wave basis set. *Comput Mater Sci* 1996;6:15–50. [https://doi.org/10.1016/0927-0256\(96\)00008-0](https://doi.org/10.1016/0927-0256(96)00008-0).
- [34] Kresse G, Furthmüller J. Efficient iterative schemes for ab initio total-energy calculations using a plane-wave basis set. *Phys Rev B* 1996;54:11169. <https://doi.org/10.1103/PhysRevB.54.11169>.
- [35] Perdew JP, Burke K, Ernzerhof M. Generalized gradient approximation made simple. *Phys Rev Lett* 1996;77:3865. <https://doi.org/10.1103/PhysRevLett.77.3865>.
- [36] Blöchl PE. Projector augmented-wave method. *Phys Rev B* 1994;50:17953. <https://doi.org/10.1103/PhysRevB.50.17953>.
- [37] Kresse G, Joubert D. From ultrasoft pseudopotentials to the projector augmented-wave method. *Phys Rev B* 1999;59:1758. <https://doi.org/10.1103/PhysRevB.59.1758>.
- [38] Methfessel M, Paxton AT. High-precision sampling for Brillouin-zone integration in metals. *Phys Rev B* 1989;40:3616. <https://doi.org/10.1103/PhysRevB.40.3616>.
- [39] Allred AL. Electronegativity values from thermochemical data. *J Inorg Nucl Chem* 1961;17:215–21. [https://doi.org/10.1016/0022-1902\(61\)80142-5](https://doi.org/10.1016/0022-1902(61)80142-5).
- [40] Clementi E, Raimondi DL, Reinhardt WP. Atomic screening constants from SCF functions. II. Atoms with 37 to 86 electrons. *J Chem Phys* 1967;47:1300. <https://doi.org/10.1063/1.1712084>.
- [41] Cordero B, Gómez V, Platero-Prats AE, Revés M, Echeverría J, Cremades E, Barragán F, Alvarez S. Covalent radii revisited. *Dalton Trans* 2008:2832–8. <https://doi.org/10.1039/b801115j>.
- [42] Borgschulte A, Terreni J, Billeter E, Daemen L, Cheng Y, Pandey A, Łodziana Z, Hemley RJ, Ramirez-Cuesta AJ. Inelastic neutron scattering evidence for anomalous H–H distances in metal hydrides. *Proc Natl Acad Sci USA* 2020;117:4021–6. <https://doi.org/10.1073/pnas.1912900117>.
- [43] Momma K, Izumi F. VESTA3 for three-dimensional visualization of crystal, volumetric and morphology data. *J Appl Crystallogr* 2011;44:1272–6. <https://doi.org/10.1107/S0021889811038970>.
- [44] Zhang SB, Northrup JE. Chemical potential dependence of defect formation energies in GaAs: application to Ga self-diffusion. *Phys Rev Lett* 1991;67:2339. <https://doi.org/10.1103/PhysRevLett.67.2339>.
- [45] Dolui K, Rungger I, Pemmaraju CD, Sanvito S. Possible doping strategies for MoS₂ monolayers: an ab initio study. *Phys Rev B* 2013;88:075420. <https://doi.org/10.1103/PhysRevB.88.075420>.
- [46] Miedema AR, de Boer FR, de Chatel PF. Empirical description of the role of electronegativity in alloy formation. *J Phys F Met Phys* 1973;3:1558. <https://doi.org/10.1088/0305-4608/3/8/012>.
- [47] Loh SM, Xia X, Wilson NR, Hine NDM. Strong in-plane anisotropy in the electronic properties of doped transition metal dichalcogenides exhibited in W_{1-x}Nb_xS₂. *Phys Rev B* 2021;103:245410. <https://doi.org/10.1103/PhysRevB.103.245410>.
- [48] Hong S, Fu CL. Hydrogen in Laves phase ZrX₂ (X = V, Cr, Mn, Fe, Co, Ni) compounds: binding energies and electronic and magnetic structure. *Phys Rev B* 2002;66:094109. <https://doi.org/10.1103/PhysRevB.66.094109>.
- [49] Westlake DG. Site occupancies and stoichiometries in hydrides of intermetallic compounds: geometric considerations. *J Less Common Met* 1983;90:251–73. [https://doi.org/10.1016/0022-5088\(83\)90075-9](https://doi.org/10.1016/0022-5088(83)90075-9).
- [50] Ren XL, Shi PH, Yao BD, Wu L, Wu XY, Wang YX. Hydrogen solution in high-entropy alloys. *Phys Chem Chem Phys* 2021;23:27185–94. <https://doi.org/10.1039/D1CP04151G>.
- [51] Banerjee S, Kumar A, Pillai CGS. Improvement on the hydrogen storage properties of ZrFe₂ Laves phase alloy by vanadium substitution. *Intermetallics* 2014;51:30–6. <https://doi.org/10.1016/j.intermet.2014.02.015>.
- [52] Kandavel M, Ramaprabhu S. Semi-empirical model for enthalpy of formation and hydrogen content in Zr-based AB₂ alloys. *Int J Hydrogen Energy* 2007;32:620–5. <https://doi.org/10.1016/j.ijhydene.2006.05.017>.
- [53] Van Mal HH, Buschow KHJ, Miedema AR. Hydrogen absorption in LaNi₅ and related compounds: experimental observations and their explanation. *J Less Common Met* 1974;35:65–76. [https://doi.org/10.1016/0022-5088\(74\)90146-5](https://doi.org/10.1016/0022-5088(74)90146-5).
- [54] Shuang Z, Qin L, Ning C, Li M, Wen Y. Calculation and prediction for the hydriding properties of LaNi_{5-x}M_x alloys. *J Alloys Compd* 1999;287:57–61. [https://doi.org/10.1016/S0925-8388\(98\)00809-3](https://doi.org/10.1016/S0925-8388(98)00809-3).
- [55] Gesari SB, Pronsato ME, Visintin A, Juan A. Hydrogen storage in AB₂ Laves phase (A = Zr, Ti; B = Ni, Mn, Cr, V): binding energy and electronic structure. *J Phys Chem C* 2010;114:16832–6. <https://doi.org/10.1021/jp106036v>.